Research Article | Vol. 29, No. 23 / 8 Nov 2021 / Optics Express 37262
Optics EXPRESS

Shaping the topology of light with a moving Rabi-oscillating vortex

LORENZO DOMINICI,[1,9] NINA VORONOVA,[2,3,10] DAVID COLAS,[4] ANTONIO GIANFRATE,[1] AMIR RAHMANI,[5] VINCENZO ARDIZZONE,[1] DARIO BALLARINI,[1,6] MILENA DE GIORGI,[1] GIUSEPPE GIGLI,[1,6] FABRICE P. LAUSSY,[3,7] AND DANIELE SANVITTO[1,8]

[1]CNR NANOTEC, Istituto di Nanotecnologia, Via Monteroni, 73100 Lecce, Italy
[2]National Research Nuclear University MEPhI (Moscow Engineering Physics Institute), 115409 Moscow, Russia
[3]Russian Quantum Center, Skolkovo Innovation City, 121205 Moscow, Russia
[4]Aix Marseille Université, CNRS, Centrale Marseille, LMA UMR 7031, Marseille, France
[5]Department of Physics, Azarbaijan Shahid Madani University, Tabriz, Iran
[6]Dipartimento di Matematica e Fisica E. de Giorgi, Universitá Del Salento, Campus Ecotekne, via Monteroni, Lecce 73100, Italy
[7]Faculty of Science and Engineering, University of Wolverhampton, Wulfruna Street, WV1 1LY, UK
[8]INFN Sezione di Lecce, 73100 Lecce, Italy
[9]lorenzo.dominici@nanotec.cnr.it
[10]nsvoronova@mephi.ru

Abstract: Quantum vortices are the analogue of classical vortices in optics, Bose-Einstein condensates, superfluids and superconductors, where they provide the elementary mode of rotation and orbital angular momentum. While they mediate important pair interactions and phase transitions in nonlinear fluids, their linear dynamics is useful for the shaping of complex light, as well as for topological entities in multi-component systems, such as full Bloch beams. Here, setting a quantum vortex into directional motion in an open-dissipative fluid of microcavity polaritons, we observe the self-splitting of the packet, leading to the trembling movement of its center of mass, whereas the vortex core undergoes ultrafast spiraling along diverging and converging circles, in a sub-picosecond precessing fashion. This singular dynamics is accompanied by vortex-antivortex pair creation and annihilation and a periodically changing topological charge. The spiraling and branching mechanics represent a direct manifestation of the underlying Bloch pseudospin space, whose mapping is shown to be rotating and splitting itself. Its reshaping is due to three simultaneous drives along the distinct directions of momentum and complex frequency, by means of the differential group velocities, Rabi frequency and dissipation rates, which are natural assets in coupled fields such as polaritons. This state, displaying linear momentum dressed with oscillating angular momentum, confirms the richness of multi-component and open quantum fluids and their innate potentiality to implement sophisticated and dynamical topological textures of light.

1. Introduction

In quantum fluids and optical fields, vortex cores are point-like phase singularities, a null-density point around which the wavefunction profile rotates. Such zero-dimensional objects can become an axis of rotation extended along one direction inside a bulk space or when tracked in time on a plane. This way, they draw curves inside a multidimensional domain (*e.g.*, of real space and time, but also in the reciprocal spaces of momentum and energy). These trajectories are called wave dislocations [1], or vortex lines and, being quantized, topological strings [2,3]. Interesting examples are given by the extended networks of vortex lines inside a 3D atomic

#438035 https://doi.org/10.1364/OE.438035
Journal © 2021 Received 16 Jul 2021; revised 24 Sep 2021; accepted 13 Oct 2021; published 27 Oct 2021

Optics EXPRESS

Bose-Einstein condensate (BEC), whose configurations and reconnections give rise to different phase transitions [4–6], analogously to what happens with electrons in superconductors, or to elementary pair interactions [7] able to subtend diverse macroscopic patterns [8]. Closed loops are possible, known as vortex rings [9,10], which can even become twisted to the extent of making vortex knots [11–14], as those induced in nonlinear optical media [15]. In optics, where angular momentum quantization is pursued as a possible variable for data encoding [16–18], optical vortex beams—like Laguerre-Gauss (LG), Bessel, and Airy beams with nonzero angular momentum [19,20]—are similar possible solutions for propagation in empty space. This confers robustness to free-space communications [21,22] and finds a variety of specialized applications, such as in femtochemistry, for new selection-rules studies, or for ionized states manipulation in photoionization processes [23,24]. Also, advanced schemes for structured light have been proposed based on frozen waves [25,26], curved and solenoidal beams [27–29] with or without inner singularity, in order to realize trapping, rotational and pulling actions on small particles or objects, enriching the field of optical tweezers [30–33]. Singular beams thus provide a great potential to study topological complexity [34] and sophisticated applications, *e.g.*, in data encoding or interferometry gyroscopes.

In vectorial fields, a full description needs to be equipped with a vector charge or two dimensional-phase—prominently, transverse polarization in optics or pseudospin in multicomponent condensates—going beyond the scalar amplitude and phase of a scalar quantum fluid. The vortex core in a vector beam is not necessarily associated to a zero of the total density anymore [35,36], but it becomes a polarization singularity [37,38], and it can represent a winding around any arbitrary axis of the 2D-valued phase [39], described by means of the Poincaré sphere in the case of a polarization state. This is what happens in so-called spin-vortices, *e.g.*, hedgehog and hyperbolic textures [40], or lemon and star patterns in half-integer vortices [36,38,41], and other generalized vortices [39,42]. The vector beam can be mapped to a 0D, 1D or 2D domain [43] on the sphere, representing the set of carried pseudospin states and its codimension. One of the most notable entities in the latter class is the full Poincaré beam [44], an optical analogy of half-vortices [41] and skyrmions [39] in BECs, a sophisticated vector state that has been shown to be generated simply by the overlap of counter-polarized Laguerre-Gaussian states with a zero (LG_{00}) and unitary (LG_{01}) vortex charges. More recently, such a double-beam superposition state has been enriched with temporal dynamics thanks to the Rabi oscillations [45,46] arising in strongly-coupled systems, such as polaritons that are themselves a superposition of microcavity photons and quantum well excitons. This led to the realization of the so-called full Bloch beam [47] (FBB) with a whole pseudospin (Bloch vector) texture in the transverse plane which is also rotating and drifting in time, similarly to what has been theorized for rotating full Poincaré beams [48] and their polarization texture. As a consequence, using the natural filtering of the full-wavefunction offered by the cavity photoluminescence, rather than using a polarization filtering, the Bloch singularity was directly projected into the helicoidal dynamics of a vortex line sculpted into the light emission from the system. Full Bloch beams hosting Rabi-spiraling vortices are also endowed with time-varying orbital angular momentum (OAM), similarly to those recently generated through nonlinear phenomena [49,50]. One way to understand such structured emission is in terms of the mechanics found by Nye and Berry [1,51], who showed that photonic helical dislocations in 3D space can be ascribed to the superposition of straight vortex lines with, *e.g.*, a tilted plane wave, and to their continuously varying relative phase, due to different wavevector directions. In the case of exciton-polariton full Bloch beams, the relative phase is that between the upper and lower polariton modes, which is geometrically set by a two-pulse excitation scheme and evolving in time due to the frequency difference induced by the Rabi splitting. The resulting emitted complex light is characterized by a spiraling inner vortex tube precessing around the axis of propagation, like a gyroscope, on a sub-picosecond timescale, or an ultrafast microscopic tornado of light whose axis of rotation is spiraling itself.

Optics EXPRESS

2. Results

2.1. Polaritonic platform of coupled fields

Making use of the same polaritonic quantum-fluid platform, here we investigate the rich morphology of singularities achievable in polaritonic fields. In particular, we show that by combining the transverse linear and orbital momentum of the fluid, we are able to unfold the pseudospin texture of the system, further empowering the dynamics in the observed photonic component. Experimentally, the present study relies on a single-pulse resonant excitation that imprints a linearly moving vortex with the ultrafast tracking of its subsequent motion. While it is the internal polariton Rabi oscillations that drive the dynamics, the detection is being made via the external (emitted from the microcavity) light field, and is therefore ultimately a pure singular-optics effect. This is a convenient, effective and powerful way to shape light. With linear motion, polariton composite vortices [52] reveal additional non-trivial, counter-intuitive and peculiar features. The moving vortex is seen to start a self-oscillatory dynamics of its core and center of mass, initially spiraling out and then coming back to the center of the packet. More sophisticated features such as ultrafast cyclic vortex-antivortex pair-generation and annihilation events are observed, being the manifestation of the underlying Bloch pseudospin texture. It is important to note that while the spiraling of a vortex core as well as the creation of vortex-antivortex pairs are often observed and discussed in the context of nonlinear phenomena in optics, condensates and quantum fluids [53], here they are due to purely linear mechanisms. In essence, the strong coupling of the photon and exciton fields leads to the new normal modes of the system, the polaritons, which have two different frequencies, and these two modes contribute to building up the observable photon field and its exciton counterpart. The dynamics in the resulting fields can then be described in terms of interference concepts, when taking into account a spatially varying relative phase between the normal modes and their continuous phase shift in time due to the different energies. As a result, the OAM of the observed photonic component is oscillating, sweeping several multiples of $\hbar$, while staying conserved in the full-wavefunction state comprising the (not directly observable) exciton component. Despite the FBB homeomorphism, consisting in a stereographic projection between the Bloch sphere and the real space, being here broken, the mapping of the Bloch parameters to real space is still possible and shown to mathematically subtend all the dynamics. This work highlights the complexity of vortex strings and topological surfaces obtainable with polariton fluids when driven by the internal dynamics of a full wavefunction. We used fundamental LG-beams building blocks to realize dynamical concepts of 2D pseudospin textures and their 1D and 0D connections. The texture is realized and put into motion by the interplay of three driving effects, typical for polariton fluids, represented by the different group velocities, the differential decay and the Rabi oscillations. Future directions to explore include the implementation of such topology shaping to different platforms [54] or to even more variegated optical beams, to realise, *e.g.*, rotating vortex lattices or advanced optical tweezers with rotational feature on multiple levels, *i.e.*, spin and orbital angular momentum, and spiraling vortex cores.

2.2. Moving Rabi-oscillating vortex

The group velocity of a wavepacket represents the velocity at which both the *density* and *phase* spatial patterns move. In the case of exciton-polaritons, which are intrinsically a two-component fluid of coherently mutually-transforming excitons and photons [55,56], the new normal modes of the system—the upper and lower polaritons (UP, LP)—possess a peculiar non-parabolic energy dispersions. In particular, while the LP and UP modes have the same group velocity $(1/\hbar)\partial E(k)/\partial k$ at small in-plane momenta k, the two velocities (v_L, v_U) become distinct as the LP mode has a maximum at the inflection point of the $E(k)$ dispersion curve (see Fig. 1) [57,58]. To exploit this peculiarity, we imprint a single LG_{01} wavepacket by a femtosecond pulse at

Optics EXPRESS

the central in-plane wavevector $k_0 = 1.9\ \mu\text{m}^{-1}$, slightly above the inflection point of the LP dispersion, upon oblique incidence excitation. The spatial width of the packet is $\sigma \sim 10\ \mu$m. The central energy of the laser pulse has been blue-detuned with respect to the LP branch, in order to remain resonant with both normal modes to trigger the Rabi oscillations. As a consequence, the exciton-polariton wavepacket splits into two fluids travelling at different speeds, while at the same time carrying an intrinsic orbital angular momentum (iOAM, *i.e.*, a vortex charge). As the initially coincident UP and LP vortices start to continuously drift apart, they trigger the dynamics in which the propagating vortex cores in the photon and exciton components oscillate, displaying rotation of both their center-of-mass and the phase singularity positions.

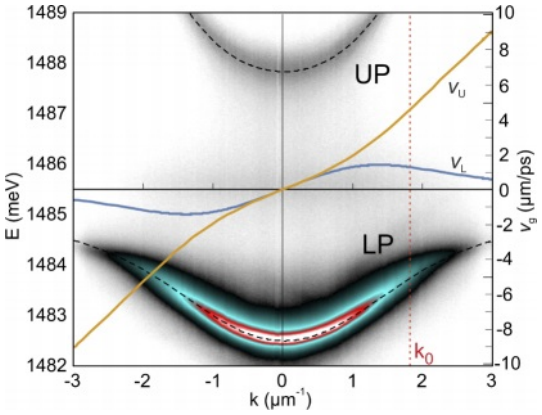

Fig. 1. Polariton modes and group velocities. Photonic emission from the polariton device under off-resonant excitation, highlighting the energy-momentum dispersion of the two normal modes, the upper and lower polariton branches. The dashed lines indicate the theoretical fitting of the dispersions $E(k)$. The modes splitting of 5.4 meV (at $k = 0$) corresponds to the Rabi period of ≈ 0.78 ps. The blue and yellow solid lines show the group velocities $v_g = (1/\hbar)\partial E(k)/\partial k$ of the LP and UP packets motion, respectively.

Before turning to the more complex early-time dynamics, we first show in Fig. 2 the full range (*i.e.*, long-time) dynamics of the moving Rabi-oscillating vortex. The wavepacket carrying a vortex can be seen propagating, preserving its shape, as shown in the amplitude maps of Fig. 2(a), taken at successive time delays of 2 ps. The Rabi oscillations together with the spatial propagation can be seen in Fig. 2(b), reporting the timespace chart of the photonic amplitude cut along the horizontal line of motion. The group velocity of the packet, extracted from the slope in such charts $v_g = 1.3\ \mu\text{m ps}^{-1}$ is in good agreement with the fitting of the LP mode dispersion, as the LP branch is the one contributing most to the emitted photon density at long times ($\geq$ 2ps), due to the faster decay of the UP mode. The full *xyt* vortex line is presented in Fig. 2(c). At early times ($\leq$ 2ps, orange lines), the initially imprinted vortex core gradually starts a (clockwise) rotational motion with increasing radius, corresponding to an increasing in-plane speed. The vortex line is broken as soon as the core gets displaced outside the density spot, during the second Rabi period, and it is replaced by a co-winding but oppositely (counter-clockwise) spiraling vortex drawn from outside of the packet ($\geq$ 2ps, red lines). The rotation direction inversion is ascribed to the inversion of the overall UP and LP populations imbalance. By tuning the laser excitation energy, the initial state was brought closer to the UP mode, *i.e.*, at early times, the system is characterized by a larger content of upper polaritons. Since they are decaying faster than the LP, at a given time, they reach equal populations. After the population reversal, the lower polaritons always dominate in the system, and the phase singularity is tracked as a continuous string. Its structure consists of a translational motion combined with the Rabi rotation, and the trajectory is a damped cycloid on the *xy*–plane. The linear movement is also associated to the whole vortex packet, with

Optics EXPRESS

the core which would reside in its centre during the propagation (in the absence of oscillations), while the Rabi-induced rotation periodically brings the vortex core inside and outside the centre.

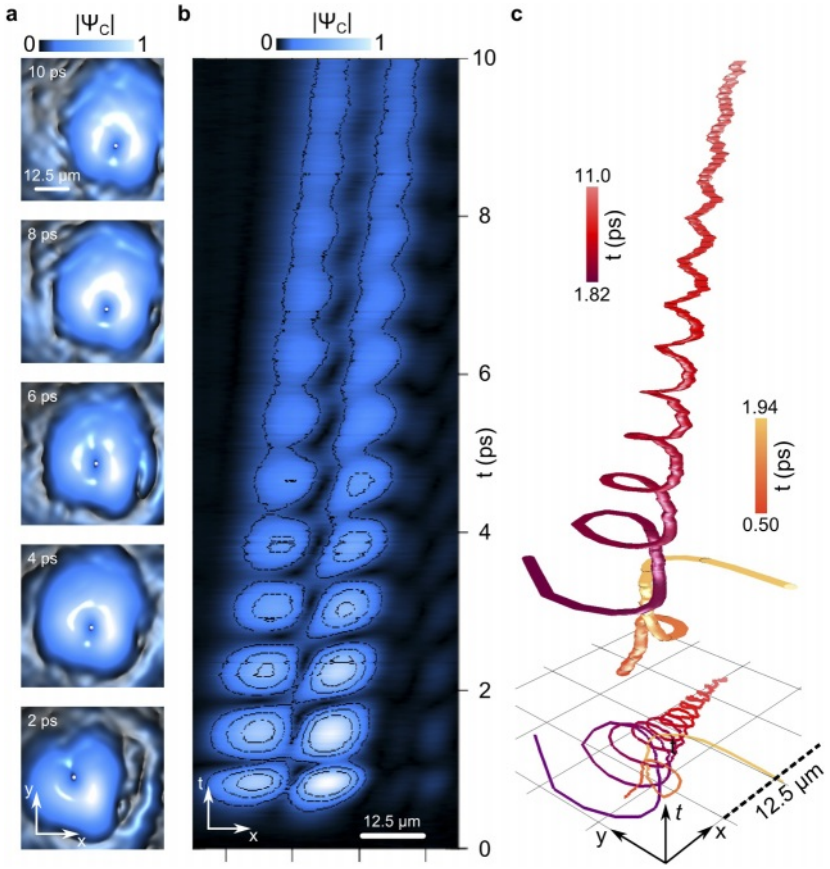

Fig. 2. Full-range dynamics of the moving Rabi-oscillating vortex. a, The xy space maps of the photonic amplitude $|\psi_C|$ at $t = 2, 4, 6, 8$ and 10 ps, as marked. **b**, Timespace chart of the photonic amplitude taken along the x direction of motion, displaying the Rabi oscillations and the spatial propagation of the vortex. **c**, Experimental vortex xyt line (time range $t = 0.5 - 11$ ps, step $\delta t = 0.02$ ps). The trajectory is broken: in the range $t = 1.82 - 1.94$ ps, two coexisting vortices are seen, the initially imprinted one being pushed to the boundary (orange curve, $0.50 - 1.94$ ps) and the one replacing it drawn to the centre of the cloud (red curve, $1.82 - 11.0$ ps). The latter vortex bears the same winding and replaces the original one, but rotates in the opposite direction. The projection on the xy–plane illustrates the damped cycloid of the phase singularity position during the vortex motion. The launching momentum corresponds to $k_0 = 1.9\ \mu\text{m}^{-1}$, and the average group velocity of the whole packet is $v_g = 1.3\ \mu\text{m ps}^{-1}$. See also Visualization 1.

2.3. *Vortex-antivortex pair creation and annihilation*

Whereas the combination of translational and Rabi-oscillatory rotational motion explains the continuous spiraling trajectory (the red line in Fig. 2(c)), the discontinuity of the vortex line requires a more careful look for the early-times dynamics which is presented in Fig. 3. In particular, the imprinted vortex core (see the bottom panel corresponding to $t = 1.80$ ps) and a further vortex entering the spot from the outside, can be simultaneously visible in the successive

Optics EXPRESS

time frames of Fig. 3(a),(b) (amplitude and phase of the photonic emission at 40 fs equispaced time frames, taken around $t \approx 2$ ps).

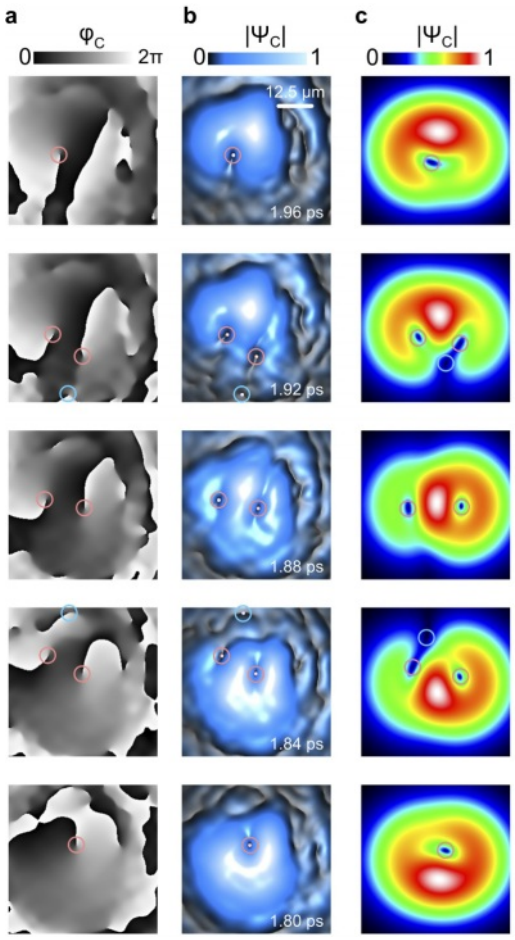

Fig. 3. Early-time dynamics. a, b, Experimental space maps of the photonic phase φ_C (a) and amplitude $|\psi_C|$ (b) of the propagating vortex shortly after the excitation (bottom to top, isospaced by 40 fs). The initial phase singularity is moved out and replaced by a core of the same charge, created close to the boundary in a V–AV pair creation process. The oppositely charged vortices which are created together with the new, and then annihilated with the original vortex are visible in the panels corresponding to $t = 1.84$ ps and 1.92 ps, respectively. **c**, The moving LG beams model reproducing the initial vortex swapping by the pair-creation and -annihilation. In all panels, the vortex and antivortex cores positions are marked with the pink and blue circles, respectively. See also Visualization 1.

This dynamics suggests that the vortex initially seen is associated to the UP wavepacket, while after its faster decay, the vortex is associated to the LP mode. In the intermediate times, two vortices with the same sign are visible. The density map does not allow to precisely track where the excess vortex is coming from. However, the phase maps suggest that the pair creation events at the boundaries play a role in the disappearance of the initial vortex and the appearance of the new one. Such events are shadowed by the sensitivity to noise of the external region of the polariton fluid bearing very low density. However the theoretical model confirms the mechanics, which is first accompanied by the appearance of a vortex-antivortex (V–AV) pair, with the AV

Optics EXPRESS

that quickly escapes the condensate spot (see the panels corresponding to $t = 1.84$ ps) leading to the simultaneous presence of the two Vs of the same charge which are neatly visible in the middle of the packet ($t = 1.88$ ps), and bringing the iOAM of the photon fluid to $2\hbar$. As shown later, the mechanism is in agreement with the presence of one open edge line able to move the AV to and from the transverse infinity and hence produce the dynamic variation of the net topological charge in the observable region of space [59]. We anticipate here and discuss later that the total OAM is conserved in the global wavefunction made of both photon and exciton fields. Soon after, the AV reappears from the opposite side of the sample ($t = 1.92$ ps), annihilating with the initially imprinted vortex and restoring the unitary topological charge of the fluid. The remaining vortex ($t = 1.96$ ps), created in the V–AV pair generation event, starts spiraling in the opposite direction, as described above. The panels in the third column, Fig. 3(c), contain a reconstruction of the photonic amplitude dynamics by means of a model overlapping the two polariton LG_{01} packets of the same width but with a different center and amplitude, and a shifting relative phase. While the first two parameters are set by the packets moving with different velocities and by their different emission rates, the geometrical relative phase cycles due to the Rabi energy splitting, as discussed in the following.

2.4. Polariton Bloch sphere mapping

We now describe the topological texture underlying the dynamics observed in the photonic component of the polariton full wavefunction created on the exciton-polariton Bloch sphere by the continuously shifting (non-coinciding) wavepackets in the two system's normal modes. The exciton component is expected to behave similarly, being in phase opposition to the photon state (see the Bloch sphere metric introduced in Fig. 4). In a perfect analogy to the Poincaré sphere for polarization, we use polar coordinates to map both the local UP-LP content imbalance and relative phase between the UP and LP fields. Similarly to the Stokes parameter s_3 [60], the content imbalance parameter $s = \frac{|\psi_U|^2 - |\psi_L|^2}{|\psi_U|^2 + |\psi_L|^2} = \cos\theta$ (θ being the polar angle) defines the latitude on the sphere, while the longitude, or azimuthal angle, is directly the relative phase $\varphi_{LU} = \varphi_U - \varphi_L$ (assuming $\psi_{L(U)} = |\psi_{L(U)}| \exp[i\varphi_{L(U)}]$). The two respective variables are represented in Fig. 4(a),(b) both as a coordinate system and by color-scale distributions on the sphere, where the metric is always fixed, while the evolution of the polariton system consists of the redistribution of the full wavefunction according to the Rabi rotation, packets motion, decay, *etc.* (for details, see Ref. [47]). At the same time, on the real plane, the respective parameters $s = s(x, y)$ and $\varphi_{LU} = \varphi_{LU}(x, y)$ are always shifting due to the change in the UP and LP wavefunctions at each point of space. We also define the global content imbalance parameter $S = \frac{\int |\psi_U|^2 d\mathbf{r} - \int |\psi_L|^2 d\mathbf{r}}{\int |\psi_U|^2 d\mathbf{r} + \int |\psi_L|^2 d\mathbf{r}}$ that characterises the system and the current shape of s mapping between the Bloch sphere and the real space at any given time. The morphology of the s and φ_{LU} maps is fundamental to understand the vortex cores dynamics. It can be stated that the vortex core in one field (here photon or exciton), being not just a phase singularity but also a density zero by definition, can only occur at a point where the normal modes (upper and lower polaritons) fully destructively interfere, *i.e.*, at the point where their amplitude is the same. For such a reason, the vortex core in the photon (or exciton) field can only move along a path which is represented by the $s(x, y) = 0$ lines. The other condition required for destructive interference is the phase difference between the base fields being $\varphi_{LU}(x, y) = 0$ (or π) for the photon (or exciton) field. The relative phase whose shape is that of a vortex dipole is then rotating due to the Rabi oscillations. In other terms, the vortex core in the photon (or exciton) field move along the isocontent orbits, according to the cyclic Rabi-oscillations drive.

Optics EXPRESS

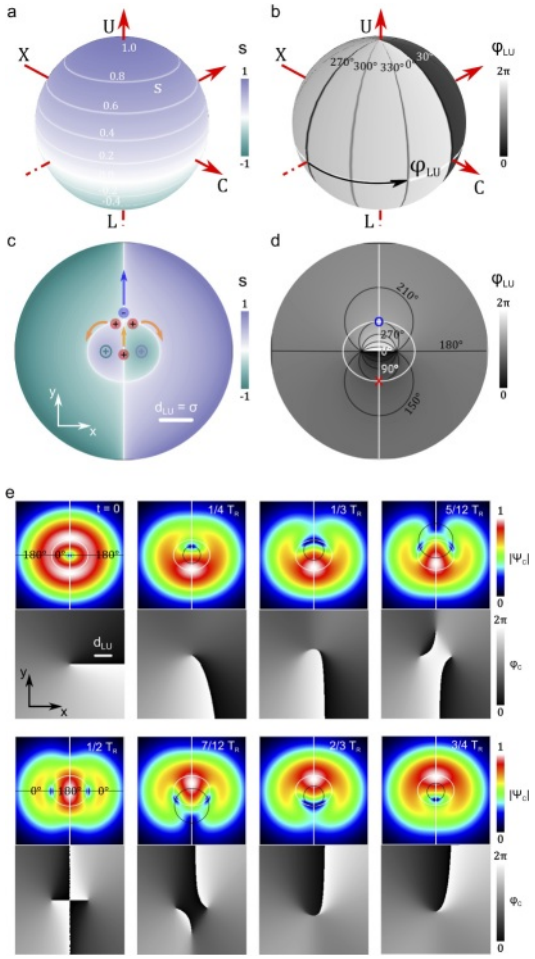

Fig. 4. Bloch sphere to real plane mapping and the V-AV pair creation/annihilation during a Rabi cycle in the symmetric content case $S = 0$. a,b, Exciton-polariton Bloch sphere, with its latitude s (a) and longitude φ_{LU} (b) coordinates and color-scale maps. **c,d**, The model real-plane maps of the local content imbalance $s(x, y)$ and relative phase $\varphi_{LU}(x, y)$. The intersecting vertical line and a loop (solid white in **c**, **d** and **e**) represent the loci of the isocontent $s = 0$ which is the trajectory of the exciton and photon vortices cores. In **c**, the red and blue dots represent the initially imprinted photonic V moving up and spliting into two Vs and an AV at the intersection point between the straight line and the loop. The LP and UP cores are marked with green and purple circles, respectively. In **d**, the φ_{LU} isolines are marked with solid black half-circles at every 30° intervals (which is a $T_R/12$ time spacing). The places for the V → 2V + AV and 2V + AV → V events are shown with the open blue circle (creation) and the red cross (annihilation). They are distant in time four isolines, $4/12\ T_R = 1/3\ T_R$ **e**, Maps of $|\psi_C|$ and φ_C at different times during one Rabi period, showing the initial photonic V moving up along the line and swapping into a charges triplet (V plus a V-AV pair). The two Vs move laterally and downwards along the circle, and the AV keeps moving up until going to infinity and then reappearing from the bottom of the straight line before annihilating with the two Vs in the last panel, ready to start the cycle again. The solid black circle represents the union of the two $(\varphi_{LU} = 0) \cup (\varphi_{LU} = \pi)$ meridians at each time.

Optics EXPRESS

2.5. Symmetric content case

The s and φ_{LU} maps, theoretically retrieved, are presented in Fig. 4(c),(d), respectively. At early times, the vortex cores in the overlapping UP and LP fluids coincide, and s is constant all over the real plane, but with time, the distance between the cores linearly increases as $d_{LU} = (v_U - v_L)t$. The distribution represented in Fig. 4(c),(d) corresponds to a given reached distance ($d_{LU} = \sigma$) between the vortices in the UP and LP components of the fluid and, for simplicity, for the case of equal global UP and LP contents ($S = 0$). It is important to point out a fundamental difference with the case of the full Bloch beam created by a double-pulse splitting of two standing vortices [47]. In the case of the FBB, the metric of meridians and parallels on the sphere is mapped to the real plane as two families of orthogonal Apollonian circles. In the current case, there is no second LG_{00} pulse shaping the normal modes packets into asymmetric, off-axis vortices. Contrary to FBB, here they remain two symmetric LG_{01} vortices, but splitting their positions in time due to the difference in group velocity of the upper and lower polaritons. On the one hand, this similarly creates a vortex dipole, but with increasing size, in the relative phase φ_{LU}, as shown in Fig. 4(d). The isophase meridians do form a circle on the sphere when taken together in pairs, ($\varphi_{LU} = \text{const}$) $\cup$ ($\varphi_{LU} = \text{const} + \pi$), and these circles are still mapped into circles in real space passing through the positions of the UP and LP vortex cores (see also Fig. 6(c)). On the other hand, the isocontent lines $s(x, y) = \text{const}$, representing the trajectories of any specific quantum state in real space, are not perfect circles anymore, and hence not everywhere orthogonal to the relative phase isolines $\varphi_{LU}(x, y) = \text{const}$. The pure photon (C) and exciton (X) are the phase-opposite states on the equator of the Bloch sphere (see Fig. 4(a), the $s = 0$ line), corresponding to the intersection of this line with the longitudes $\varphi_{LU} = 0$ and π (see Fig. 4(b)). The isocontent lines on the real plane, $s(x, y) = 0$, shown in white in the Fig. 4(c)-(e), map the trajectories followed by the C (X) vortex cores which, being null-density points in the respective fields, are the only points in space hosting their pure X (C) counterpart. The Rabi oscillations, corresponding to the full-wavefunction rotation on the Bloch sphere, are understood as a continuous drift of the isophase lines on the plane that allows to track the dynamics of the vortex cores moving along the $s(x, y) = 0$ lines following the intersection with the isophases $\varphi_{LU} = \pi$ or 0. Here, contrary to the case of the standing FBB state, the shape and size of the vortex core orbits are not fixed, but change in time even in the conservative case of no decay (*i.e.*, when $S = \text{const}$), due to the relative movement.

2.6. Three-charges events

We first show for clarity the mechanics in the ideal case of both the absence of decay and of frozen packets, where the relative movement is suppressed (but after they already have split by some distance). As a consequence, the effective dynamics retrieved by the theory for the photonic amplitude $|\psi_C|$ (or, similarly, the exciton amplitude $|\psi_X|$), their phase and vortex cores in the symmetric $s(x, y)$ situation is shown in Fig. 4(e) at significant time frames during one Rabi-oscillation period T_R. To track the C (or X) vortex cores motion, one needs to follow the intersection of the $s(x, y) = 0$ isocontent line, representing the motion trajectories, with the isophase $\varphi_{LU}(x, y) = \pi$ (or 0) in time, representing the motion drive induced by the Rabi rotation of the full wavefunction on the Bloch sphere. In the present case, there are two nodal points of the isocontent line with itself (*i.e.*, such a line is composed by the intersecting loop and straight line), so that there are two points of trajectory bifurcation. As a result, these positions become singular points where the V-AV pairs creation and annihilation events periodically happen. In fact, both V and AV in the photon field share the same property in the basis of the normal modes, being a zero of the respective field and lying on the same equatorial point of the Bloch sphere. The consequence is that a vortex in the centre that is moving upward would split (precisely at the time $t = 1/3\ T_R$) into two vortices going left and right and an anti-vortex that continues to go up. The AV is seen going to infinite distance ($y \to \infty$), coming back at a successive time from the

Optics EXPRESS

opposite direction ($y \to -\infty$), after which the three vortex charges annihilate (at $t = 2/3\ T_R$, as also seen from the relevant isophase line in Fig. 4(d)), leaving one resulting vortex in the center. The creation and annihilation events are hence separated in time by $\Delta t = (2/3 - 1/3)\ T_R = 1/3\ T_R$, while the experimental sequence in Fig. 3 is comprised in a 0.16 ps time interval, which is $1/5\ T_R$. Such a difference can be ascribed to the varying separation d_{LU} between the lower and upper vortex cores, which is fixed and equal to the packet width σ in the model case, while it has only reached a lower value (roughly estimated to be less than $0.65\ \sigma$) in the experiments. Such a distance influences the orbits shape, as discussed in the following section, and also affects the positions and time at which V-AV pair events take place. It is noteworthy that while there are always two vortices in the normal modes' relative phase φ_{LU}, and either one or three vortices at a time in a single bare mode (*i.e.*, photon or exciton), there are either two or four singularities in the relative phase between the bare modes [$\varphi_{CX}(x, y)$, not shown]. In such a phase map, the two orbital splitting points said above represent two saddle points [61,62], and the specific $(\varphi_{CX} = \pi/2) \cup (\varphi_{CX} = 3\pi/2)$ isoline concides with the $s = 0$ isocontent line shown in Fig. 4.

2.7. Relative decay and asymmetric dynamics

In the experiments, while the vortex dipole in the relative phase profile expands due to the gradual drifting apart of the LP and UP vortex cores during their motion, the local imbalance parameter $s(x, y)$ redistributes due to both the wavepackets motion and the differential decay of the two modes, $\gamma_{LU} = \gamma_U - \gamma_L \approx \gamma_U$ (the decay rates are introduced as $|\psi_{L(U)}(t)| = \exp[-\gamma_{L(U)}t]|\psi_{L(U)}(0)|$). The interplay of the two effects is also reflected on the photon (and exciton) vortex core orbits which initially gradually expand, reach a maximum size and then shrink back. Figure 5(a) shows the model maps of $s(x, y)$ for the case of larger, equal, and smaller total UP to LP content ($S>0$, $S = 0$, and $S<0$, top, middle, and bottom row panels, respectively). Each column of the table corresponds to increasing relative distances between the vortex cores in the system's normal modes (whose packets appear in Fig. 5(b)). The figure illustrates symmetric and asymmetric local imbalance maps corresponding to different situations, in particular, to the evolution of the $s = 0$ lines that are the trajectories of the photon and exciton vortex cores motion (white lines in the maps, separating domains of $s>0$ and $s<0$). They are composed of a closed ring and a bent open line (*i.e.*, the line closed at infinite distance) that eventually intersect and merge (in some panels, they become two closed loops and one open line). Conditions for their intersection and detachments are described in a previous work on the positioning of polarization singularities [60]. In the case of the moving polariton vortex packets, their evolution is due to the linear increase of the relative distance d_{LU} in time and the global population imbalance S decrease according to the exponential decay of the two polariton components, yielding $S(t) = \tanh\{-\gamma_{LU}t - \mathrm{atanh}[S(0)]\}$. The actual evolution of the $s(x, y)$ maps is hence the sequence of maps following the lines overlapping the table of frames in Fig. 5(a) (cyan, blue and black solid lines), given by different γ_{LU} or $S(0)$.

In the symmetric case of Fig. 4, the cores dynamics comprises a three-charges event, which in reality is rarely observed as the balance of total populations, providing the symmetric case $S = 0$, is reached only once during the evolution and then is instantly lost. The dynamics in a more realistic case of the asymmetric distribution (both $S>0$ and $S<0$) is shown in Fig. 6(a),(b). While one initially imprinted ("main") vortex core is moving along a closed loop on one side of the polariton cloud, the separated line, also mapping the Bloch sphere equator, hosts the two-charges events. Subsequent vortex-antivortex pair creation and annihilation (marked with the open circle and cross marks, respectively) are happening at different times of the Rabi period. The loci of these events and their time spacing can be understood when overlapping the $s = 0$ isocontent (white solid) lines with the vortex dipole in the relative phase profile, as shown in Fig. 6(c). It is where the isophase lines are tangent to the isocontent [or, in other terms, $\boldsymbol{\nabla}\varphi_{LU} \perp \hat{\boldsymbol{s}}_{orbit}$, with $\hat{\boldsymbol{s}}_{orbit}$ the local versor of the $s(x, y) = 0$ line] that the V-AV pairs are generated and annihilated.

Optics EXPRESS

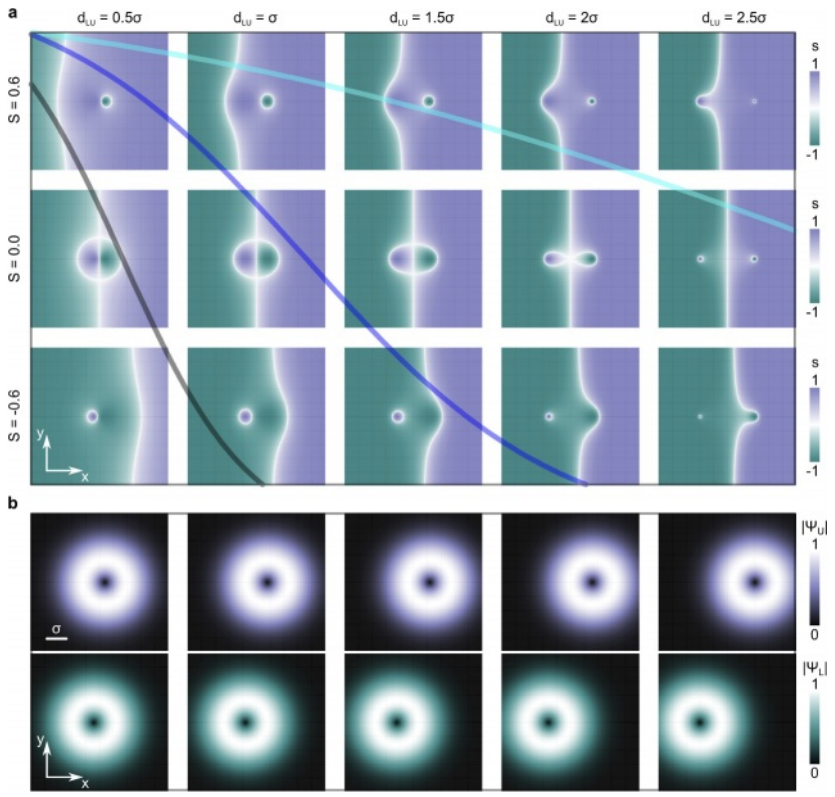

Fig. 5. Local imbalance maps and polariton vortex packets. **a**, Local imbalance real-space maps $s(x, y)$ for different cores displacements d_{LU} (columns) and global imbalances S (rows). The C (X) vortex cores move, driven by the Rabi rotation of the polariton full wavefunction on the Bloch sphere, along the line $s(x, y) = 0$ (white lines). While the distance d_{LU} changes in time linearly, the evolution of the global imbalance parameter S assumes the hyperbolic tangent shape. Therefore, the real dynamics effectively follows the maps along the overlapped solid lines (the specific line depends on the initial value of S defined by the excitation laser and on the $(v_U - v_L)/\sigma$ to γ_{LU} ratio). **b**, Schematics of the moving LP and UP LG_{01} wavepackets for different relative distances d_{LU} (according to the same column ordering as in **a**). For the sake of representation, panels in both **a** and **b** are centered with respect to the moving middle of the vortex dipole $x_0 = (v_U - v_L)t/2$ (*i.e.*, the UP and LP vortices are always positioned symmetrically). See Visualization 2.

Optics EXPRESS

The created antivortex is accelerating to an infinite speed and goes to infinite distance before coming back from the opposite direction of the cloud to participate in the annihilation process. However, the photonic vortex cores are only visible inside the packet density, which is fading down with distance and time. The time interval between the pair creation and annihilation events is evaluated as $1/4\ T_R$ (if S and distance d_{LU} are kept constant) by counting the isophase lines between them. From the previous Fig. 5(a) it can be inferred that, in different situations, not only the orbits but also the timing of the V-AV events is changed, depending on the isocontent and isophase lines' relative positions and their intersections. At smaller separations d_{LU}, the time interval of the V-AV pairs existence is reduced.

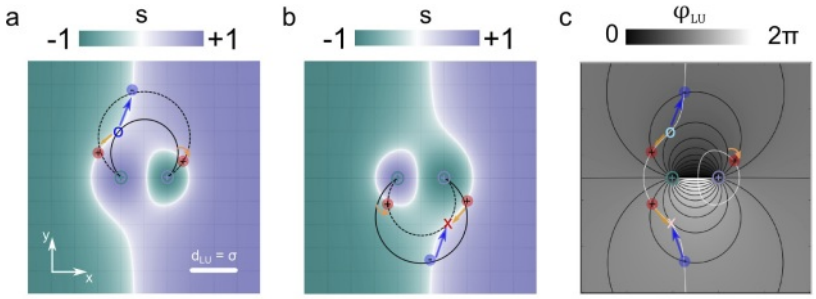

Fig. 6. Photon vortex cores orbits and V-AV pair dynamics in the general case $S \neq 0$. **a,b**, $s(x, y)$ maps with S>0 (0.18, **a**) and S<0 (-0.18, **b**). The main (originally imprinted) vortex is circulating along the closed $s = 0$ loop (white loop). While the main vortex charge maintains the same initial sign (*e.g.*, positive), its core moves in the opposite directions in the two respective cases. The V-AV pair creation and annihilation cyclically happen on the open branch of the $s = 0$ isocontent, in the two different halves of the Rabi period, and are shown with the open blue circle (creation) and the red cross (annihilation) on the maps. **c**, $\varphi_{LU}(x, y)$ map showing that these events happen in the spatial positions where the relative isophase lines (represented by the solid black line, with a $2\pi/24$ spacing) are tangent to the vortex trajectory (white solid line). As an example, the solid and dashed black lines in **a,b** represent the circular arc of $\varphi_{LU} = 0$, at a given time and after $T_R/24$, respectively. The pair events in the case of a constant $S = 0.18$ are shown in **c** as distant in time six isolines, equal to $6/24\ T_R = 1/4\ T_R$. The LP and UP cores are marked with green and purple circles, respectively. When considering together the Rabi cycle and the differential decay, the orbital motion is following the orbit reshaping, and the dynamics can evolve from panel **a** to panel **b**, with the main vortex swapping from the right to the left side during the population inversion (S crossing zero), as in the experiments of Fig. 3. See also Visualization 2.

2.8. Topology of the isocontent surface

The dynamics of the vortex cores within the evolution of the population imbalance and relative phase of the normal modes represent an exemplary case of complex light, involving singular beams, group velocities, Rabi oscillations and the Bloch sphere mapping. The complexity of the topology can be represented as surfaces and lines in a 3D space when considering the xyt domain. In Fig. 7, we present the model isocontent surface $s_{=0}(x, y, t)$, from different angles of perspective for clarity. In the bottom panel it is evident that at the initial time, the LP and UP vortex cores are overlapped and start to separate as straight lines (green and purple, respectively) with their relative linear movement. The change with time of the global content imbalance S gives rise to the diverging and converging cone wrapped around such vortex lines generator, with the inversion of one cone into the other at the merging of the two surfaces. The photonic main vortex core is shown (red dots) spiraling around the two opposite cones at different time intervals. On the other hand, the secondary vortex-antivortex pairs (red and blue dots, respectively) are

Optics EXPRESS

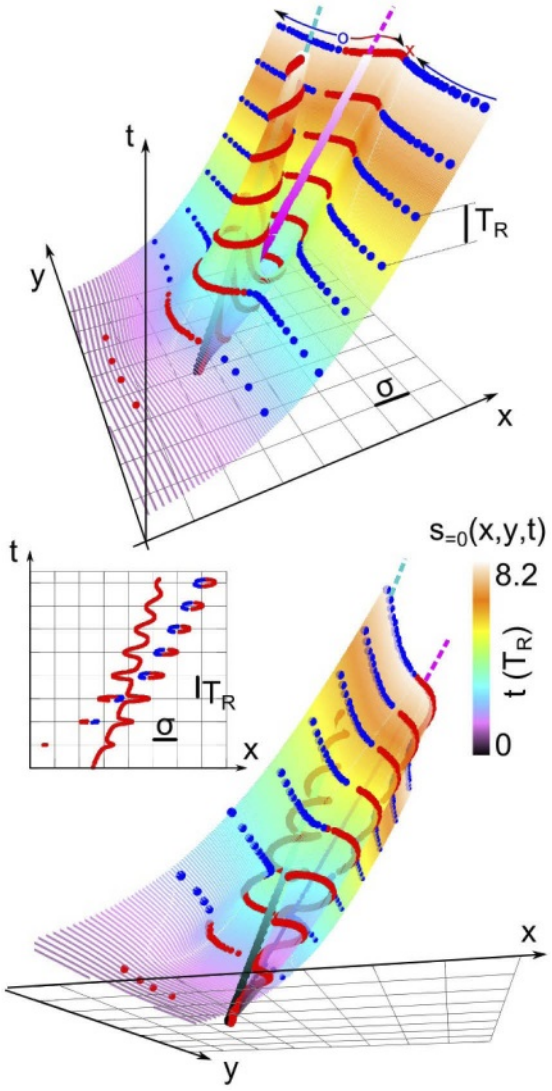

Fig. 7. Topology of the $s = 0$ isocontent lines as an *xyt* surface. a, b, The two plots depict two projections of the evolution of the isocontent lines $s(x, y) = 0$ as a function of time (vertical axis). The two views are from the top and bottom of the *xy*–plane, for the sake of clarity. The cone surface visible on the bottom panel is emerging from a point-like source which represents the initially overlapped vortex core in the UP and LP fields (purple and green lines, respectively), splitting in time and enlarging this cone. The cone visible in the top panel represents the isocontent line wrapping around the slower moving vortex core in the LP mode. The main charge (red dots) is initially circling around the bottom cone and then passing to the top one, with opposite spiraling directions. The opposite charges (red and blue dots for V and AV, respectively) which are cyclically created and annihilated (blue circle and red cross in the top panel) move on the flatter surfaces following the direction of the arrows. The dynamics are represented with respect to the absolute frame of reference, (*i.e.*, their tilt to the right side is due to the vortex packets velocity). The dashed lines are a continuation to the LP and UP cores straight trajectories, added for clarity. The inset represents an *xt* projection, where the V–AV lines appear as closed loops.

Optics EXPRESS

present on the open branch of the $s = 0$ surface. Each pair belongs to what in reality are unitary and continuous vortex lines in the *xyt* domain. They appear as a pair creation and annihilation events when intersecting such lines with the time sequence of space-like foliations [62,63] (*i.e.*, in the *xy* surfaces), see also the loops in the inset in Fig. 7 for a different projection. The almost horizontal slope of the trajectories and the rarefaction of the dots, seen at the positions of high flatness of the surface, implies their very fast speed in the *xy*–plane, to be contrasted with the slow velocity in the high curvature regions of the cones. It should be noted that none of the vortex lines represent a null density of the full-wavefunction, that is, $|\psi_L|^2 + |\psi_U|^2$ is nowhere zero. Each vortex core is a phase singularity and a zero density in the associated field (C or X or any other). This is only one example of the topological complexity at reach with simple fundamental blocks of singular LG beams when powered into a platform of strongly coupled fields. It represents a basic scheme for understanding sophisticated topological concepts and more advanced ways of dynamically shaping complex light, which also involves the oscillations of OAM.

2.9. OAM oscillations

Finally, since the dynamics of photonic-mode projection of the polariton full wavefunction features vortex core self-oscillations and cyclic two- or three-charges events, as described above, the photoluminescence from the microcavity possesses a periodically changing topology (*i.e.*, a combination of angular momentum oscillations with the linear momentum of the moving vortex). In this section, we present the oscillations which are seen in the average OAM of the emitted light $\langle L_z \rangle_C$. In Fig. 8(a), we report the experimental case (the same as in Fig. 2 and Fig. 3(a),(b) with an initial negative vortex charge) while in Fig. 8(b),(c) the numerical case (starting with a positive vortex and in absence of damping) is shown. We have used a fixed point, which is the initial photonic vortex core position, as a pole with respect to which we compute the OAM. In the case of a symmetric vortex beam, the OAM would consist of the iOAM (the initially imprinted vortex charge) only, and would remain quantized and constant, independently from the pole with respect to which it is computed. Here, the cyclical movement of the vortex core position outside and inside the moving packet is instead associated with the changes in the total OAM due to its varying extrinsic component. In the case of a single vortex, the total OAM with respect to a specific point o (such as the initial position) can be written as $\boldsymbol{L}_o = \boldsymbol{L}_i + \boldsymbol{r}_{oi} \times \langle \boldsymbol{k} \rangle$, where $\boldsymbol{L}_i$ is the quantized and constant iOAM computed with respect to the instantaneous vortex core, $\boldsymbol{r}_{oi}$ is the position vector of the core with respect to the fixed point, and $\langle \boldsymbol{k} \rangle$ the mean transverse linear momentum (per particle). For a standing symmetric vortex beam, $\boldsymbol{r}_{oi}$ is constant in time and $\langle \boldsymbol{k} \rangle$ is null due to symmetry. However, here they both change due to the spiraling and the translation velocity. While the spiraling alone would lead to the oscillating OAM, which can only be reduced below the quantized charge value, the joint effect of the increasing distance with the asymmetric reshaping makes the $\langle L_z \rangle_C$ oscillations sweep over several values of the quantized unit $\hbar$, see Fig. 8(a),(c). The total OAM at the same time is conserved if one considers the full wavefunction, composed of both the photon and exciton fields (or, otherwise, upper and lower polariton modes, see the straight horizontal line in Fig. 8(c)).

The oscillating OAM observed in the emitted photonic component of the moving Rabi-oscillating vortex is another exemplary case of the time-varying OAM [50]. It is interesting to note that the OAM oscillations are initially growing and then decreasing due to the population imbalance, see Fig. 8(a), similarly to what was previously observed in the FBB case [47]. Here, due to the combination of OAM oscillations with the linear momentum, we observe in the emitted light $\langle L_z \rangle_C$ going over $5\hbar$ during the dynamics, converging with time to the initially imprinted unitary charge ($-\hbar$ in the experimental case and $+\hbar$ in the model case) due to the differential decay. As in any interference effect, the modulation is in fact maximum when the two fields have equal amplitudes, which is reached when $S = 0$. However, in the present case, there is also the effect of the relative movement which is changing the spatial overlap between the two packets

Optics EXPRESS

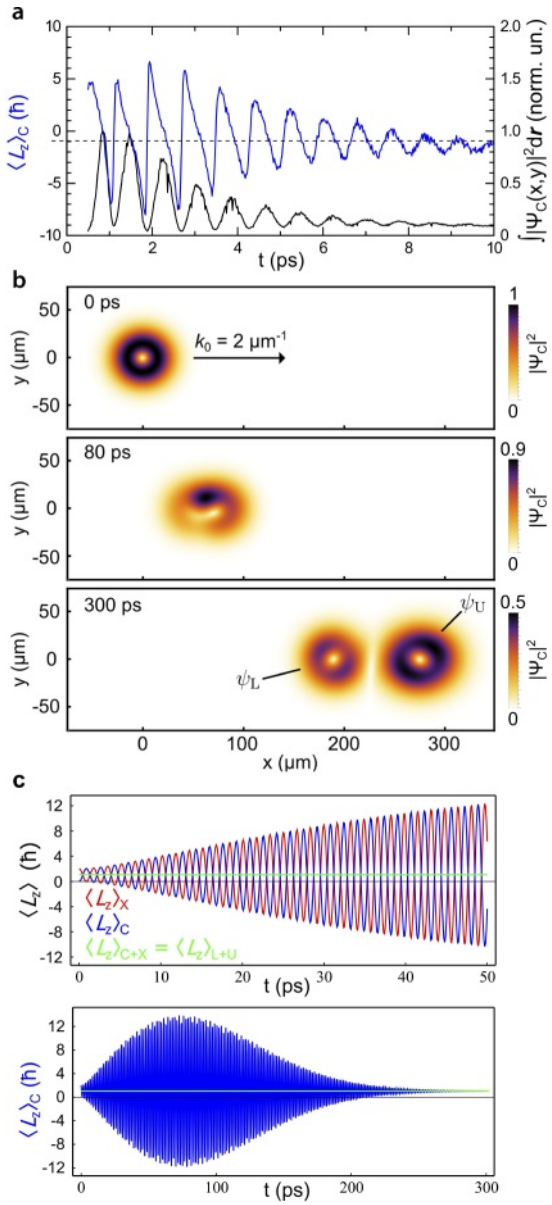

Fig. 8. Mean OAM evolution. **a**, The average OAM $\langle L_z \rangle_C$ in the experimental photon field as a function of time, left axis, and total photon population (area integrated density), right axis. The OAM is computed with respect to the fixed pole represented by the initial vortex core position. **b**, Moving Rabi-oscillating vortex modelisation showing the photon density $|\psi_C|^2$ at three different times of the vortex motion (t = 0 ps, 80 ps, and 300 ps) based on coupled Schrödinger equations. At later times, the vortices in the LP and UP components get completely separated, losing the overlap. **c**. Top: OAM expectation value of the different fields (C in red, X in blue) versus time. The net OAM (green line) is conserved. Bottom: OAM for the photonic field only, computed for larger times. It evolves with the change of the spatial overlap between the LP and UP shown in **b**. The initial OAM per particle is $-\hbar$ in the experimental case and $+\hbar$ in the model case. See also Visualization 3.

Optics EXPRESS

(Fig. 8(b)), hence altering the modulation strength and oscillations in both the bare C,X fields density and OAM. Indeed, in the theoretical ideal case of no decay which is shown in Fig. 8(c), one sees amplification of OAM oscillations up to $\pm 12\hbar$, which then decay because of the gradual separation of the UP and LP wavepackets. It should be underlined that such amplification from $\hbar$ to over $12\hbar$ happens without any nonlinearity at play, but only because of the interplay of the Rabi oscillations and the differential group velocities of the two normal modes of the system.

3. Conclusions and perspectives

We have investigated the concepts at the basis of full Bloch and full Poincaré beams by implementing ultrafast moving vortices into a planar two-component fluid of polaritons. The experimental results consist of an overall moving photon vortex core, spiraling along diverging and converging circles, and additional secondary vortex-antivortex pair-creation and -annihilation events cyclically taking place during the fluid's Rabi oscillations. This behavior leads to the periodically changing angular momentum directly observable in the light emitted from the device, oscillating in the presented case with an amplitude exceeding $5\hbar$. The modeling of the dynamics confirms the nature of the observed phenomenology as relying on the overlap of the two polariton modes bearing a spatially-varying population imbalance and a geometrical phase difference, in the shape of a vortex dipole, both evolving in time due to their different group velocity, the differential decay of the modes and the Rabi oscillations, hence interfering in such a structured way. The mapping of the polariton Bloch sphere surface to the real space is not homeomorphic. It has been shown in the previous FBB case how such bijective topological mapping could subsist and coincide with a conformal stereographic projection between the sphere and the plane in the case of a superposition of concentric LG_{00} and LG_{01} beams of the same width [44,47]. In the present case, that special situation is destroyed by the fact that the wavepackets are moving with different velocities so that the centres of the two UP/LP LG_{01} profiles become displaced. On the contrary to the homeomorphism, the current situation leads to the degeneracy of multiple real space points which are mapped to the very same polariton state, *i.e.*, point on the sphere. Such a situation is indeed physically observed by tracking a secondary vortex-antivortex pair, created and subsequently annihilated, in the emitted light, where each cores of V and AV, being a zero of the photon field, represents the pure excitonic state. More complex situations are within reach with the case of multiple charge imprinting or vortex lattices, or by adding the polarization control thus making dynamical full Poincaré beams. Using for example two opposite unitary charges (LG_{0+1} and LG_{0-1}) in the UP and LP modes would lead to the same isocontent morphologies but with the relative phase being that of a double charge rather than a dipole. A vortex core would be seen starting to orbit in the photon (or exciton) field, this time around both the LP and UP vortex cores, and an antivortex slowly coming into the packet to replace it at long times, after a transition time of the two orbiting each other. Implications touching the concepts of topology and Berry curvature will be shown in further works, while the possible use for optical tweezers, particles sorting, data encoding and interferometry gyroscopes remain to be investigated.

4. Methods

Experimental methods. The polariton device used here is fabricated by means of MBE technique and consists in an AlGaAs 2λ MC with three $In_{0.04}Ga_{0.96}As$ quantum wells of 8 nm placed at the antinodes of the cavity mode field. The cavity is placed inside two distributed Bragg reflectors made of 21 and 24 pairs of alternated $\lambda/4$ AlAs and GaAs layers. The experiments are performed in a region of the sample clean from defects. The device is kept at a temperature of 10 K inside a closed-loop He cryostat. The resonant beam is a 130 fs pulse laser with 80 MHz repetition rate and a 8 nm bandwidth. The central energy is tuned at approximately 833.5 nm in order to overlap both the LP and UP branch energies at the selected finite momentum. The photonic beam is passed through a q-plate device [64,65], in order to obtain a unitary optical vortex which is sent

Optics EXPRESS

onto the microcavity sample at oblique incidence. The polariton sample modes splitting is 3 nm (5.4 meV) at zero momentum which converts into a Rabi period of $T_R = 0.780$ ps while the T_R at the finite momentum of the experiments is slightly lesser. Once imprinted, the polariton vortex is free to move and evolve. The lifetime of the normal modes is $\tau_L = 1/\gamma_L \sim 10$ ps and $\tau_U = 1/\gamma_U \sim 2$ ps for the lower and upper modes, respectively. An ultrafast time resolved detection scheme is based on the off-axis digital holography, where the emission from the sample plane is focused on an imaging camera together with a reference beam. The reference pulse is derived by the resonant laser beam and is not focused but passed through a small iris, so that it becomes a homogeneous and flat front when arriving on the camera. The digital fast Fourier transform (FFT) filtering is applied to the interferograms and this procedure allows to reconstruct the amplitude and phase of the emitted photonic wavefunction. The FFT filtering can be applied directly in the laboratory in order to aid for the setting of the measurements. For additional details on both the polariton sample and digital holography technique see Refs. [45–47] and descriptions therein.

Numerical methods. The model is set by use of the two LG_{01} packets moving with different velocities, representing the upper and lower polariton fields. The bare exciton and photon fields are retrieved as linear combination of the normal modes. We write the spatial profiles of the fields in complex polar coordinates (r, ϕ), where $r = |x + iy|$ and $\phi = \arg(x + iy)$. The fields are written as $\psi_{U,L} = A_{U,L} e^{-|\boldsymbol{r}-\boldsymbol{r}_{U,L}|^2/2\sigma^2} \frac{|\boldsymbol{r}-\boldsymbol{r}_{U,L}|}{\sigma} e^{i \arg(\boldsymbol{r}-\boldsymbol{r}_{U,L})} e^{ik_0 x} e^{(i\omega_{U,L}-\gamma_{U,L})t}$.

The motion of the two packets is simulated by updating the distance to the centres of the beams with their group velocities $\boldsymbol{r}_{U,L}(t) = \boldsymbol{v}_{U,L} t$, assumed to be along the x-axis. The simple model gives the same results than would be derived with a full coupled Schrödinger equations (cSE) model, apart from neglecting the dispersion and diffraction effects and the initial transient from the incoming photon pulse being injected into the polariton components. We are not interested in the sub-ps transient and the beams are wide enough in order to neglect any dispersive/diffraction effects in the 10 ps time scale range. Assuming a zero detuning between the cavity photon to exciton mode, the bare modes are hence obtained as $\psi_{C,X} = (\psi_U \pm \psi_L)/\sqrt{2}$. For completeness, the cSE model has been used to verify the behavior of the moving Rabi-oscillating vortex, of the same kind as described in [47], and adding the initial central momentum k_0 to the photonic LG_{01} resonant pulse.

Funding. Russian Foundation for Basic Research (joint with CNR, Project No. 20–52–7816); Ministero dell'Istruzione, dell'Università e della Ricerca (PRIN project InPhoPol); Ministero dell'Istruzione, dell'Università e della Ricerca (CUP: B83B17000010001, delibera CIPE n. 3449 del 7/08/2017, FISR MIUR CNR, TECNOMED); Regione Puglia (CUP: B84I18000540002, DGR n. 2117 del 21/11/2018, TecnoMed Puglia); Iran National Science Foundation (97009377).

Acknowledgments. We would like to thank Romuald Houdré and Alberto Bramati for the microcavity sample, Lorenzo Marrucci and Bruno Piccirillo for the q-plate devices.

Disclosures. The authors declare no conflicts of interest.

Data availability. Data underlying the results presented in this paper are not publicly available at this time but may be obtained from the authors upon reasonable request.

References

1. J. F. Nye and M. V. Berry, "Dislocations in Wave Trains," Proc. Roy. Soc. A **336**(1605), 165–190 (1974).
2. G. E. Volovik, *The universe in a helium droplet*, no. 117 in International series of monographs on physics (Oxford University, Oxford, 2009).
3. W. H. Zurek, "Cosmological experiments in superfluid helium?" Nature **317**(6037), 505–508 (1985).
4. G. P. Bewley, M. S. Paoletti, K. R. Sreenivasan, and D. P. Lathrop, "Characterization of reconnecting vortices in superfluid helium," Proc. Natl. Acad. Sci. **105**(37), 13707–13710 (2008).
5. E. A. L. Henn, J. A. Seman, G. Roati, K. M. F. Magalhaes, and V. S. Bagnato, "Emergence of Turbulence in an Oscillating Bose-Einstein Condensate," Phys. Rev. Lett. **103**(4), 045301 (2009).
6. L. Kondaurova, V. L'vov, A. Pomyalov, and I. Procaccia, "Structure of a quantum vortex tangle in 4 He counterflow turbulence," Phys. Rev. B **89**(1), 014502 (2014).

Optics EXPRESS

7. L. Dominici, R. Carretero-González, A. Gianfrate, J. Cuevas-Maraver, A. S. Rodrigues, D. J. Frantzeskakis, G. Lerario, D. Ballarini, M. De Giorgi, G. Gigli, P. G. Kevrekidis, and D. Sanvitto, "Interactions and scattering of quantum vortices in a polariton fluid," Nat. Commun. **9**(1), 1467 (2018).
8. H. J. Zhao, V. R. Misko, J. Tempere, and F. Nori, "Pattern formation in vortex matter with pinning and frustrated intervortex interactions," Phys. Rev. B **95**(10), 104519 (2017).
9. G. W. Rayfield and F. Reif, "Quantized Vortex Rings in Superfluid Helium," Phys. Rev. **136**(5A), A1194–A1208 (1964).
10. K. O'Holleran, M. J. Padgett, and M. R. Dennis, "Topology of optical vortex lines formed by the interference of three, four, and five plane waves," Opt. Express **14**(7), 3039–3044 (2006).
11. J. Leach, M. R. Dennis, J. Courtial, and M. J. Padgett, "Vortex knots in light," New J. Phys. **7**, 55 (2005).
12. M. R. Dennis, R. P. King, B. Jack, K. O'Holleran, and M. J. Padgett, "Isolated optical vortex knots," Nat. Phys. **6**(2), 118–121 (2010).
13. D. Kleckner and W. T. M. Irvine, "Creation and dynamics of knotted vortices," Nat. Phys. **9**(4), 253–258 (2013).
14. D. Kleckner, L. H. Kauffman, and W. T. M. Irvine, "How superfluid vortex knots untie," Nat. Phys. **12**(7), 650–655 (2016).
15. A. S. Desyatnikov, D. Buccoliero, M. R. Dennis, and Y. S. Kivshar, "Spontaneous knotting of self-trapped waves," Sci. Rep. **2**(1), 771 (2012).
16. E. Nagali, L. Sansoni, F. Sciarrino, F. De Martini, L. Marrucci, B. Piccirillo, E. Karimi, and E. Santamato, "Optimal quantum cloning of orbital angular momentum photon qubits through Hong-Ou-Mandel coalescence," Nat. Photonics **3**(12), 720–723 (2009).
17. J. Leach, B. Jack, J. Romero, A. K. Jha, A. M. Yao, S. Franke-Arnold, D. G. Ireland, R. W. Boyd, S. M. Barnett, and M. J. Padgett, "Quantum Correlations in Optical Angle-Orbital Angular Momentum Variables," Science **329**(5992), 662–665 (2010).
18. R. Fickler, G. Campbell, B. Buchler, P. K. Lam, and A. Zeilinger, "Quantum entanglement of angular momentum states with quantum numbers up to 10010," Proc. Natl. Acad. Sci. **113**(48), 13642–13647 (2016).
19. A. E. Willner, J. Wang, and H. Huang, "A Different Angle on Light Communications," Science **337**(6095), 655–656 (2012).
20. S. Franke-Arnold, L. Allen, and M. Padgett, "Advances in optical angular momentum," Laser Photonics Rev. **2**, 299–313 (2008).
21. M. Krenn, J. Handsteiner, M. Fink, R. Fickler, R. Ursin, M. Malik, and A. Zeilinger, "Twisted light transmission over 143 km," Proc. Natl. Acad. Sci. **113**(48), 13648–13653 (2016).
22. C. Paterson, "Atmospheric Turbulence and Orbital Angular Momentum of Single Photons for Optical Communication," Phys. Rev. Lett. **94**(15), 153901 (2005).
23. C. T. Schmiegelow, J. Schulz, H. Kaufmann, T. Ruster, U. G. Poschinger, and F. Schmidt-Kaler, "Transfer of optical orbital angular momentum to a bound electron," Nat. Commun. **7**(1), 12998 (2016).
24. A. Picón, J. Mompart, J. R. Vázquez de Aldana, L. Plaja, G. F. Calvo, and L. Roso, "Photoionization with orbital angular momentum beams," Opt. Express **18**(4), 3660 (2010).
25. A. H. Dorrah, M. Zamboni-Rached, and M. Mojahedi, "Controlling the topological charge of twisted light beams with propagation," Phys. Rev. A **93**(6), 063864 (2016).
26. M. Zamboni-Rached, "Carving beams of light," Opt. Lett. **46**(6), 1205–1208 (2021).
27. M. M. Rahman, A. A. Sayem, M. R. C. Mahdy, M. E. Haque, R. Islam, S. T.-u.-R. Chowdhury, and M. A. Matin, "Tractor beam for fully immersed multiple objects: Long distance pulling, trapping, and rotation with a single optical set-up," Ann. Phys. (Berlin) **527**(11-12), 777–793 (2015).
28. J. Zhao, I. D. Chremmos, D. Song, D. N. Christodoulides, N. K. Efremidis, and Z. Chen, "Curved singular beams for three-dimensional particle manipulation," Sci. Rep. **5**(1), 12086 (2015).
29. S.-H. Lee, Y. Roichman, and D. G. Grier, "Optical solenoid beams," Opt. Express **18**(7), 6988–6993 (2010).
30. K. Dholakia, M. MacDonald, and G. Spalding, "Optical tweezers: the next generation," Phys. World **15**(10), 31–35 (2002).
31. T. A. Nieminen, G. Knöner, N. R. Heckenberg, and H. Rubinsztein-Dunlop, "Physics of Optical Tweezers," in *Methods in Cell Biology*, vol. 82 (Elsevier, 2007), pp. 207–236.
32. M. Padgett and R. Bowman, "Tweezers with a twist," Nat. Photonics **5**(6), 343–348 (2011).
33. K. Dholakia and T. Čižmár, "Shaping the future of manipulation," Nat. Photonics **5**(6), 335–342 (2011).
34. M. Soskin, S. V. Boriskina, Y. Chong, M. R. Dennis, and A. Desyatnikov, "Singular optics and topological photonics," J. Opt. **19**(1), 010401 (2017).
35. J. F. Nye and J. V. Hajnal, "The wave structure of monochromatic electromagnetic radiation," Proc. R. Soc. Lond. A **409**(1836), 21–36 (1987).
36. M. V. Berry, "Geometry of phase and polarization singularities illustrated by edge diffraction and the tides," in *Second International Conference on Singular Optics (Optical Vortices): Fundamentals and Applications*, vol. 4403 M. S. Soskin and M. V. Vasnetsov, eds., International Society for Optics and Photonics (SPIE, 2001), pp. 1–12.
37. M. R. Dennis, K. O'Holleran, and M. J. Padgett, "Optical Vortices and Polarization Singularities," in *Progress in Optics*, vol. 53 (Elsevier, 2009), pp. 293–363.
38. F. Cardano, E. Karimi, L. Marrucci, C. de Lisio, and E. Santamato, "Generation and dynamics of optical beams with polarization singularities," Opt. Express **21**(7), 8815–8820 (2013).

Optics EXPRESS

39. S. Donati, L. Dominici, G. Dagvadorj, D. Ballarini, M. De Giorgi, A. Bramati, G. Gigli, Y. G. Rubo, M. H. Szymańska, and D. Sanvitto, "Twist of generalized skyrmions and spin vortices in a polariton superfluid," Proc. Natl. Acad. Sci. **113**(52), 14926–14931 (2016).
40. F. Manni, Y. Léger, Y. G. Rubo, R. André, and B. Deveaud, "Hyperbolic spin vortices and textures in exciton-polariton condensates," Nat. Commun. **4**(1), 2590 (2013).
41. Y. Rubo, "Half vortices in exciton polariton condensates," Phys. Rev. Lett. **99**(10), 106401 (2007).
42. G. Liu, D. W. Snoke, A. Daley, L. N. Pfeiffer, and K. West, "A new type of half-quantum circulation in a macroscopic polariton spinor ring condensate," Proc. Natl. Acad. Sci. **112**(9), 2676–2681 (2015).
43. D. Lopez-Mago, "On the overall polarisation properties of Poincaré beams," J. Opt. **21**(11), 115605 (2019).
44. A. M. Beckley, T. G. Brown, and M. A. Alonso, "Full Poincaré beams," Opt. Express **18**(10), 10777–10785 (2010).
45. L. Dominici, D. Colas, S. Donati, J. P. Restrepo Cuartas, M. De Giorgi, D. Ballarini, G. Guirales, J. C. López Carreño, A. Bramati, G. Gigli, E. del Valle, F. P. Laussy, and D. Sanvitto, "Ultrafast control and Rabi oscillations of polaritons," Phys. Rev. Lett. **113**(22), 226401 (2014).
46. D. Colas, L. Dominici, S. Donati, A. A. Pervishko, T. C. Liew, I. A. Shelykh, D. Ballarini, M. de Giorgi, A. Bramati, G. Gigli, E. d. Valle, F. P. Laussy, A. V. Kavokin, and D. Sanvitto, "Polarization shaping of Poincaré beams by polariton oscillations," Light: Sci. Appl. **4**(11), e350 (2015).
47. L. Dominici, D. Colas, A. Gianfrate, A. Rahmani, V. Ardizzone, D. Ballarini, M. De Giorgi, G. Gigli, F. P. Laussy, D. Sanvitto, and N. Voronova, "Full-Bloch beams and ultrafast Rabi-rotating vortices," Phys. Rev. Res. **3**(1), 013007 (2021).
48. Y. Krasnoshchekov, V. Yaparov, and V. Taranenko, "Rotating full Poincaré beams," Ukr. J. Phys. Opt. **18**(1), 1–8 (2017).
49. X. Ma, Y. V. Kartashov, T. Gao, L. Torner, and S. Schumacher, "Spiraling vortices in exciton-polariton condensates," Phys. Rev. B **102**(4), 045309 (2020).
50. L. Rego, K. M. Dorney, N. J. Brooks, Q. L. Nguyen, C.-T. Liao, J. San Román, D. E. Couch, A. Liu, E. Pisanty, M. Lewenstein, L. Plaja, H. C. Kapteyn, M. M. Murnane, and C. Hernández-García, "Generation of extreme-ultraviolet beams with time-varying orbital angular momentum," Science **364**(6447), eaaw9486 (2019).
51. M. V. Berry, J. F. Nye, and F. J. Wright, "The Elliptic Umbilic Diffraction Catastrophe," Phil. Trans. R. Soc. Lond. A **291**(1382), 453–484 (1979).
52. N. S. Voronova and Y. E. Lozovik, "Excitons in cores of exciton-polariton vortices," Phys. Rev. B **86**(19), 195305 (2012).
53. L. Dominici, G. Dagvadorj, J. M. Fellows, D. Ballarini, M. D. Giorgi, F. M. Marchetti, B. Piccirillo, L. Marrucci, A. Bramati, G. Gigli, M. H. Szymańska, and D. Sanvitto, "Vortex and half-vortex dynamics in a nonlinear spinor quantum fluid," Sci. Adv. **1**(11), e1500807 (2015).
54. V. Grillo, G. C. Gazzadi, E. Mafakheri, S. Frabboni, E. Karimi, and R. W. Boyd, "Holographic Generation of Highly Twisted Electron Beams," Phys. Rev. Lett. **114**(3), 034801 (2015).
55. A. V. Kavokin, J. J. Baumberg, G. Malpuech, and F. P. Laussy, *Microcavities*, Series on Semiconductor Science and Technology (Oxford University, Oxford, 2017).
56. T. Byrnes, N. Y. Kim, and Y. Yamamoto, "Exciton–polariton condensates," Nat. Phys. **10**(11), 803–813 (2014).
57. A. Gianfrate, L. Dominici, O. Voronych, M. Matuszewski, M. Stobińska, D. Ballarini, M. De Giorgi, G. Gigli, and D. Sanvitto, "Superluminal X-waves in a polariton quantum fluid," Light: Sci. Appl. **7**(1), e17119 (2018).
58. D. Colas and F. P. Laussy, "Self-Interfering Wave Packets," Phys. Rev. Lett. **116**(2), 026401 (2016).
59. G. Molina-Terriza, L. Torner, E. M. Wright, J. J. García-Ripoll, and V. M. Pérez-García, "Vortex revivals with trapped light," Opt. Lett. **26**(20), 1601–1603 (2001).
60. D. Lopez-Mago, B. Perez-Garcia, A. Yepiz, R. I. Hernandez-Aranda, and J. C. Gutiérrez-Vega, "Dynamics of polarization singularities in composite optical vortices," J. Opt. **15**(4), 044028 (2013).
61. J. F. Nye, J. V. Hajnal, and J. H. Hannay, "Phase saddles and dislocations in two-dimensional waves such as the tides," Proc. R. Soc. Lond. A **417**(1852), 7–20 (1988).
62. M. V. Berry, "Much ado about nothing: optical distortion lines (phase singularities, zeros, and vortices)," in *International Conference on Singular Optics*, vol. 3487 M. S. Soskin, ed., International Society for Optics and Photonics (SPIE, 1998), pp. 1–5.
63. I. Freund, "Critical foliations," Opt. Lett. **26**(8), 545–547 (2001).
64. L. Marrucci, C. Manzo, and D. Paparo, "Optical Spin-to-Orbital Angular Momentum Conversion in Inhomogeneous Anisotropic Media," Phys. Rev. Lett. **96**(16), 163905 (2006).
65. E. Karimi, B. Piccirillo, E. Nagali, L. Marrucci, and E. Santamato, "Efficient generation and sorting of orbital angular momentum eigenmodes of light by thermally tuned q-plates," Appl. Phys. Lett. **94**(23), 231124 (2009).